Resonance Damping of LCL Filters Using Capacitor-Current Proportional-Integral Positive Feedback Method for Grid-Integrated Fuel Cell System

Majid Hosseinpour
Department of Electrical and Computer Engineering, University of Mohaghegh Ardabili, Ardabil. Iran, hoseinpour.majid@uma.ac.ir

Amin kholousi
Department of Electrical and Computer Engineering, University of Mohaghegh Ardabili, Ardabil. Iran, amin_kholousi@student.uma.ac.ir

1. Introduction

In recent years, renewable energy sources have become more popular because of environmental concerns and the rapid depletion of fossil fuels. The advantages of renewable energy sources include their sustainability, affordability, and reliability. Fuel cells are becoming increasingly popular among renewable energy sources because of their flexibility, silent operation, high performance, and modular construction [1]. Furthermore, fuel cells increase the system performance in terms of power regulation and stabilization compared to the intermittent operation of wind and solar energy sources [2]. There are numerous types of fuel cells used in grid-connected applications, including proton exchange membrane fuel cells (PEMFC), solid oxide fuel cells (SOFC), alkaline fuel cells (AFC), direct methanol fuel cells (DMFC), phosphoric acid fuel cells (PAFC) and molten carbonate fuel cells (MCFC). The PEMFC and SOFC are the most widely used types of fuel cells in grid-connected systems [3].

Fuel cells integrated with electrical grids are known as grid-connected fuel cell systems. In [4], the coupling problems of PEMFC in the grid-connected system have been investigated by developing an overall model integrating electrochemical, mechanical, and electrical components. In [5], a partial feedback linearizing controller is proposed for a three-phase grid-tied PEMFC system to inject power into grid under different load conditions and maintain stability during load changes and faults in the system. In [6], a novel grid-connected inverter control strategy is presented under harmonic and unbalanced grid voltage conditions. In [7], PEMFC is used as a distributed power generation system (DPG) and converter side current feedback (CSCF) method is used in its control system. DPGs are commonly used in low-power distribution systems, so grid inductance variations should be considered during control design. LCL filters are widely used in DPG applications. In the weak power distribution system, the converter side current feedback (CSCF) method has been used to connect the fuel cell system through the LCL filter to the network.

Grid-connected inverters are very significant in DPG systems. PWM switching causes these inverters to have high-frequency harmonics [8]. In comparison to conventional L filters, LCL filters are more effective at reducing switching effects and eliminating switching harmonics [9-10]. However, the inherent resonance of the LCL filter complicates the design of the current controller in low-voltage grid connections. Consequently, the control loop bandwidth can be reduced, and even the system stability could be threatened [11-12]. Using damping methods is an effective way of reducing resonance caused by LCL filters and stabilizing the system. A simple way is to connect damping resistors in series with filter capacitors, known as the passive damping method. While this method is simple and very reliable, it causes a lot of power losses and is not very effective at attenuating harmonics [13]. Passive damping (PD) can be replaced with active damping (AD), which simulates a virtual resistance with variable feedback as the damping condition. These feedbacks include filter capacitor current feedback (CCF) [14], filter capacitor voltage feedback [15], inverter side current feedback [16], or grid side current feedback [17]. Due to its flexibility and

efficiency, AD has become widely used [18], but additional sensors are usually required to measure the variables associated with AD.

According to [19], the CCF will be proportional to virtual impedance when computational and PWM delays are considered in one-and-a-half sample periods, respectively. This virtual impedance has a negative real component from one-sixth to one-half of the sampling frequency [f_{sam}/6, f_{sam}/2] and gives rise to right-half plane (RHP) poles. RHP leads to a non-minimum phase behavior in the system [20]. According to [19], the f_{sam}/6 frequency is the critical frequency for LCL resonance, and stability is maintained at frequencies greater or smaller than f_{sam}/6. Thus, if the resonance frequency changes due to variations in network impedance, the control system becomes unstable. A simple solution to this problem is reducing the delay of digital computations. In order to prevent RHP, the frequency range of the positive equivalent resistance causing a minimum phase behavior can be extended by reducing or compensating control delays [21-23]. Among AD methods based on the feedback of filter state variables, proportional CCF damping has been widely used due to its simple implementation. In this method, double loop control is used to dampen the LCL resonance effectively.

In this paper, an LCL filter is utilized to connect the PEMFC to the power transmission grid. By using the AD method based on capacitor-current positive feedback (CCPF), the frequency range of the positive virtual equivalent resistance can be extended up to the Nyquist frequency, and the LCL filter resonance damping can also be increased. This damping method uses the equivalent output virtual impedance of the grid-connected inverter to increase system stability and robustness. Using the proposed control system, the grid-connected inverter will have high stability against changes in grid impedance and remain stable during variations in the PEMFC-produced power.

The rest of the paper is organized as follows: In the second part, a general description of the system, a mathematical model, and AD based on CCF are examined. The principles of AD performance based on proportional-integral CCPF are presented in the third part. The fourth section is dedicated to the design of CCF parameters and current regulator values. Detailed analysis of sample design and simulation results are discussed in the fifth section, and finally, the paper's conclusion is presented in section six.

2. General description of the system and active damping based on capacitor-current feedback

2. 1. Description of the system and mathematical modeling

Fig. 1 presents the structure of a fuel cell system connected to a single-phase network using an LCL filter. In this figure, L_1, C, and L_2 form the LCL filter, and V_g represent the grid voltage. An inductor typically represents the network impedance at a point of common coupling (PCC). Because network resistance improves damping and contributes to system

stability, a pure inductor L_g is considered to indicate the worst grid condition. Also, to increase the voltage level and connect the fuel cell to the grid, a DC-DC converter is used.
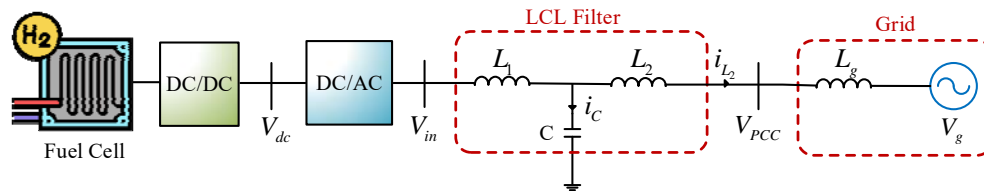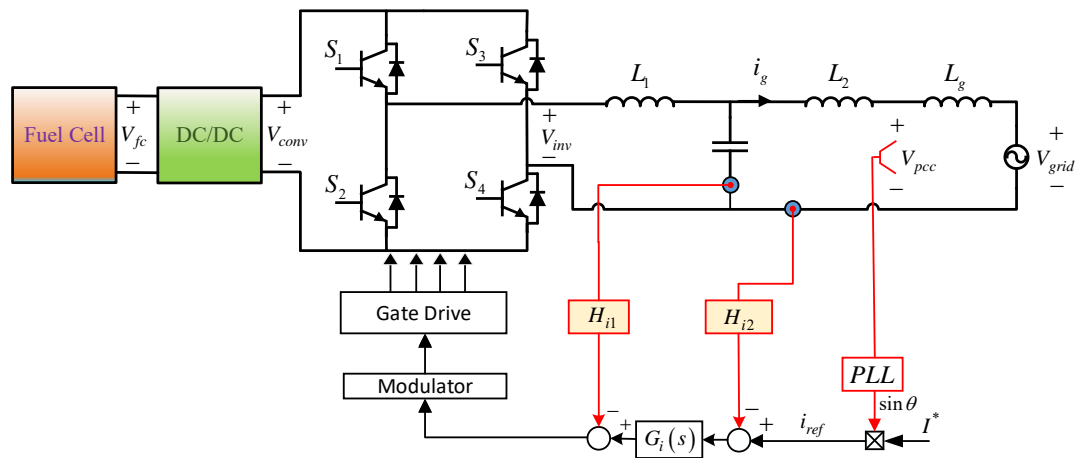

Fig. 1: System outline

Fig. 2: Proposed control scheme for grid-connected fuel cell system using LCL filter

Fig. 2 provides a detailed schematic of the grid-connected inverter equipped with the LCL filter. H_{i2} represents the gain of the grid-side current. In order to dampen the resonance peak of the LCL filter, the capacitor current feedback active damping method with H_{i1} coefficient as the capacitor current sensor gain has been considered. The grid-connected inverter employs unipolar pulse width modulation (SPWM) as its switching pattern, and $G_i(s)$ is the current regulator. The reference grid-side current is denoted as i_{ref}, with phase-locked loop (PLL) synchronization used to align this current with the voltage at the common coupling point (V_{pcc}). A power control loop automatically adjusts the amplitude of the reference grid-side current, denoted as I*.

Based on the outline of the system under consideration, as shown in Fig. 2, the block diagram of the grid-connected inverter control using the LCL filter by applying damping resonance based on CCF is demonstrated in Fig. 3. Grid-connected inverters are designed to regulate the injected current to the grid (i_{L2}) sinusoidally and to regulate its phase using the point of common coupling voltage. Therefore, a phase-locked loop (PLL) is used to derive the phase angle of the V_{PCC}. Additionally, the reference current amplitude is calculated by setting the DC link voltage as I*. $G_i(s)$ presents the current regulator. To determine the damping resonance of the LCL filter, the I_C capacitor-current is measured.

H_{i1} and H_{i2} are the i_C and i_{L2} gains, respectively. The inverter transfer function is modeled by $K_{PWM} = V_{inv} / V_{tri}$. Here, V_{tri} represents the peak of the triangular carrier amplitude, and V_{inv} represents the peak AC voltage generated by the inverter.

$G_d(s)$ indicates computational and PWM delays, which can be expressed as follows:

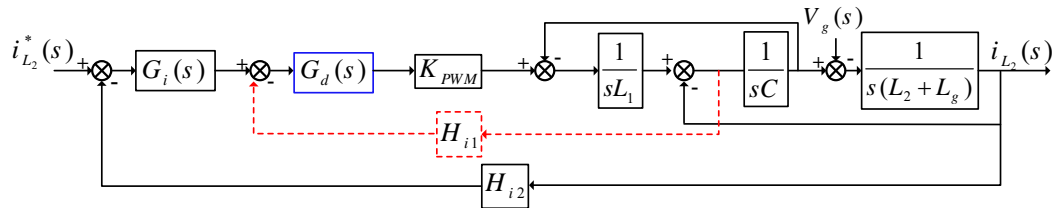$$G_d(s) \approx e^{-1.5sT_s} \tag{1}$$

Fig. 3: Digital control diagram of the grid-connected inverter with LCL filter and proportional capacitor-current AD

In this case, T_s represents the sampling period. The proportional resonant controller (PR) is used in the following equation to minimize the steady-state error:

$$G_i(s) = K_p + \frac{2K_r \omega_i s}{s^2 + 2\omega_i s + \omega_o^2} \tag{2}$$

K_p indicates the proportional gain, and K_r is the resonant gain, $\omega_0 = 2\pi f_0$ is the principal component of the grid angular frequency, where ω_i indicates the bandwidth of the resonance section that reduces the sensitivity to changes in the main frequency.

In Fig. 3, the gain of the $T(s)$ loop, which is the open-loop transfer function, is determined as follows:

$$T(s) = \frac{H_{i2}G_i(s)}{sL_1(L_2 + L_g)C} \cdot \frac{K_{pwm}G_d(s)}{s^2 + s \cdot H_{i1}K_{pwm}G_d(s)/L_1 + \omega_r^2} \tag{3}$$

ω_r is the resonant frequency angle of the LCL filter, which is expressed as follows:

$$\omega_r = 2\pi f_{res} = \sqrt{\frac{L_1 + L_2 + L_g}{L_1(L_2 + L_g)C}} \tag{4}$$

2. 2. Single-Loop control of the grid current

The stability of the grid-connected inverter is usually evaluated by the Nyquist stability criterion according to the Z = P-2(N(+)-N(-)) equation. P and Z represent the number of right half-plane poles (RHP) of the open loop and closed loop transfer functions, correspondingly. Further, N(-) and N(+) indicate the number of negative and positive passes of -180 degrees, respectively. The necessary and sufficient condition for stability is Z=0.

Fig. 4 illustrates the Bode diagram of equation (3). When $H_{i1} = 0$, AD is not taken into account, and T(s) does not contain any open-loop poles in the right half-plane (RHP), i.e., P = 0. Nyquist stability requires N(+) - N(-) = 0 for the system to be stable. Under various values of L_g, Fig. 4 displays T(s) without AD. According to this figure, there is a uniform decrease in the phase-frequency curve, so N(+) = 0. If $f_{res} \leq f_{sam}/6$, the negative passage happens in f_{res}, so N(-) =1, meaning stability has not been achieved. If $f_{sam}/6 < f_{res} < f_{sam}/2$, the curve of phase-frequency for T(s) passes through -180 degrees at $f_{sam}/6$ because of the phase delay caused by $G_d(s)$. As a result of the phase delay generated by $G_d(s)$, the curve of phase-frequency for T(s) passes through -180 degrees at $f_{sam}/6$ if $f_{sam}/6 < f_{res} < f_{sam}/2$. Additionally, this will not be a negative pass when the T(s) gain at $f_{sam}/6$ is lower than zero dB. By adjusting the proportional gain K_P, this can be accomplished.

Substituting $s = j2\pi f_{sam}/6$ at (3) and assuming $|T(j2\pi f_{sam}/6)| < 0$ dB, the following Equation is obtained:

$$K_p < \frac{L_1(L_2 + L_g)C}{H_{i2}K_{pwm}} \cdot 2\pi \frac{f_{sam}}{6} \left[(2\pi f_{res})^2 - (2\pi \frac{f_{sam}}{6})^2 \right] \tag{5}$$

This means that reducing the proportional gain will ensure system stability, but may compromise dynamic performance [24].
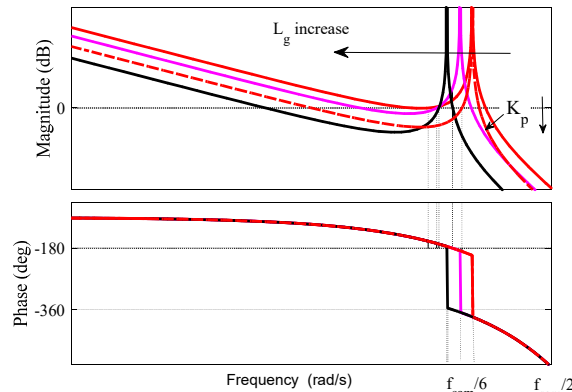

Fig. 4: Bode diagram of single-loop current control loop gain

According to the analysis, maintaining the LCL resonant frequency within the $[f_{sam}/6, f_{sam}/2]$ range is a simple method to ensure inverter stability against changes in grid impedance. This can be achieved by replacing the inverter side inductor and the filter capacitor resonant frequency as $f_{r\infty}$, higher than $f_{sam}/6$. Actually, $f_{r\infty}$ is the LCL resonant frequency when L_g is a large-value inductor. Simplicity makes this method interesting, but it is critical to design the LCL filter carefully [25]. Accordingly, for low-voltage consumer applications, iron powder cores are commonly used in filter inductors. Due to the soft permeability, the value of the filter inductors varies in a wide range. Considering that the minimum value of inductor L_1 determines the permissible current ripple for the inductor, in this case, the condition $f_{r\infty} > f_{sam}/6$ needs to be met under the maximum value of inductor L1, making it necessary to use

a reasonably small capacitor C. Due to the harmonic reduction of the switching frequency, L_2 may be a relatively large and bulky filter. Comparatively, when damping is applied, the $f_{r\infty} > f_{sam}/6$ condition is unnecessary, so the choice of filter parameters is much easier and helps to minimize the filter size. Here, a suitable damping method is investigated.

2. 3. Active damping based on capacitor-current feedback

AD of proportional CCF has attracted much attention due to its simplicity. Using the variations depicted in Fig. 5(a), the proportional CCF AD, according to Fig. 5(b), is equivalent to a virtual Z_{eq} impedance parallel to the filter capacitor C. The virtual impedance equivalent to Z_{eq} is expressed as follows:

$$Z_{eq}(s) = \frac{L_1}{H_{i1}K_{pwm}C} \cdot \frac{1}{G_d(s)} \tag{6}$$

By considering (1) and substituting $s = j\omega$ in (6), the equation (7) can be obtained.

$$Z_{eq}(\omega) = \frac{L_1}{H_{i1}K_{pwm}C} \cdot \frac{1}{e^{-1.5j\omega T_s}} = \frac{L_1}{H_{i1}K_{pwm}C} \cdot e^{1.5j\omega T_s} \square R_{eq}(\omega) \| jX_{eq}(\omega) \tag{7}$$

In which:

$$R_{eq}(\omega) = \frac{L_1}{H_{i1}K_{pwm}C\cos(1.5\omega T_s)} \tag{8}$$

$$X_{eq}(\omega) = \frac{L_1}{H_{i1}K_{pwm}C\sin(1.5\omega T_s)} \tag{9}$$

According to Equation (7) and Fig. 5(b), Z_{eq} can be represented as a parallel connection of the R_{eq} resistor and X_{eq} reactance. Both the R_{eq} and X_{eq} parameters are frequency-dependent. R_{eq} helps attenuation damping, and X_{eq} makes the system resonant frequency (f_{res}) different from the filter resonant frequency (f_r').

The frequency properties of R_{eq} and X_{eq}, when H_{i1} is positive, are displayed in Fig. 6, according to (8) and (9). As shown in the figure, R_{eq} has a positive value in the [0, $f_{sam}/6$] and a negative value in the [$f_{sam}/2$, $f_{sam}/6$] frequency range. Additionally, X_{eq} has a capacitive behavior in the [$f_{sam}/2$, $f_{sam}/3$] frequency range. Conversely, in cases where H_{i1} is negative, R_{eq} has a negative value in the [0, $f_{sam}/6$] and a positive value in the [$f_{sam}/2$, $f_{sam}/6$] frequency range. Besides, X_{eq} has capacitive behavior in the [0, $f_{sam}/3$] and inductive behavior in the [$f_{sam}/2$, $f_{sam}/3$] frequency range.
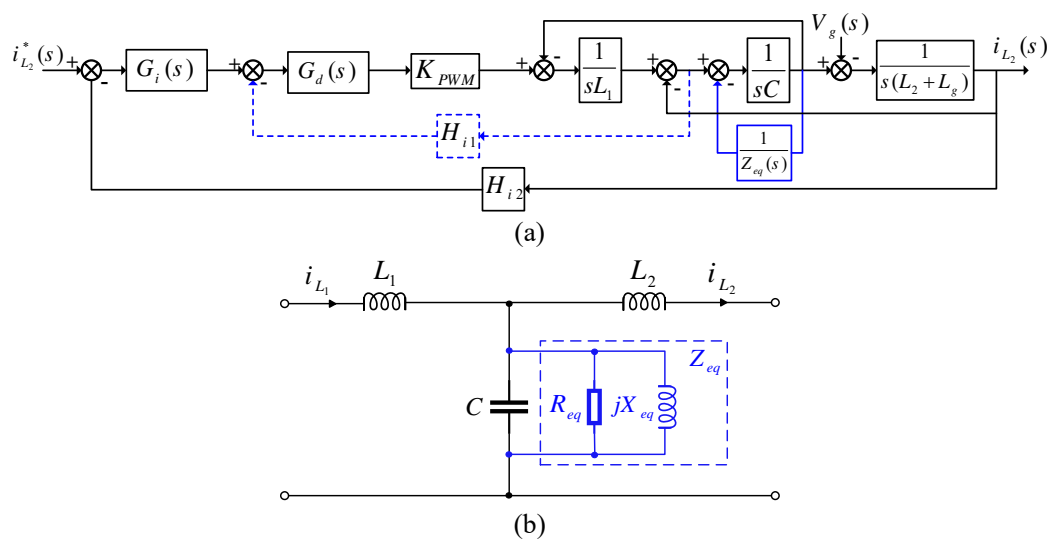
(a)

(b)

Fig. 5: Inverter diagram with proportional AD capacitor-current, (a) schematic diagram, (b) equivalent circuit

Based on the previous analysis and the results of [26], it is not important whether H_{i1} be positive or negative, what matters is that the equivalent resistance value be positive in the [0, fsam/2]. If the $R_{eq}(f_r')$ be negative in the [0, f$_{sam}$/2] frequency range, the system will be unstable. Therefore, it is necessary to use a suitable damping method to ensure that R_{eq} is positive in the whole [0, f$_{sam}$/2] desired frequency range. Under these conditions, the stability of the inverter against network impedance changes increases significantly.
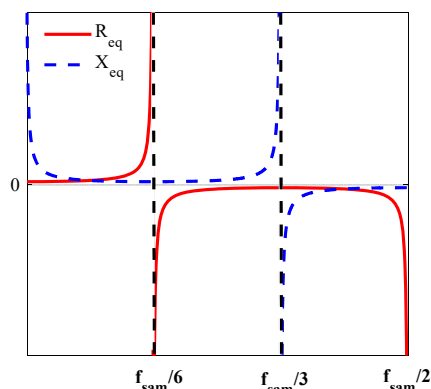

Fig. 6: Frequency characteristic of R_{eq} and X_{eq} when $H_{i1} > 0$

3. Active damping using proportional-integral capacitor-current positive feedback

3. 1. Basic concepts

To achieve a positive equivalent resistance across the controllable frequency range, a simple idea, as shown in Fig. 7(a), is to add a feedback function in parallel with H_{i1}. Through block equivalent conversion, this additional feedback is equivalent to a Z_p impedance connected via a parallel connection to the primary Z_{eq} equivalent impedance. Fig. 7(b) demonstrates the equivalent circuit of the grid-connected inverter considering the additional virtual impedance Z_p.

(a)

(b)
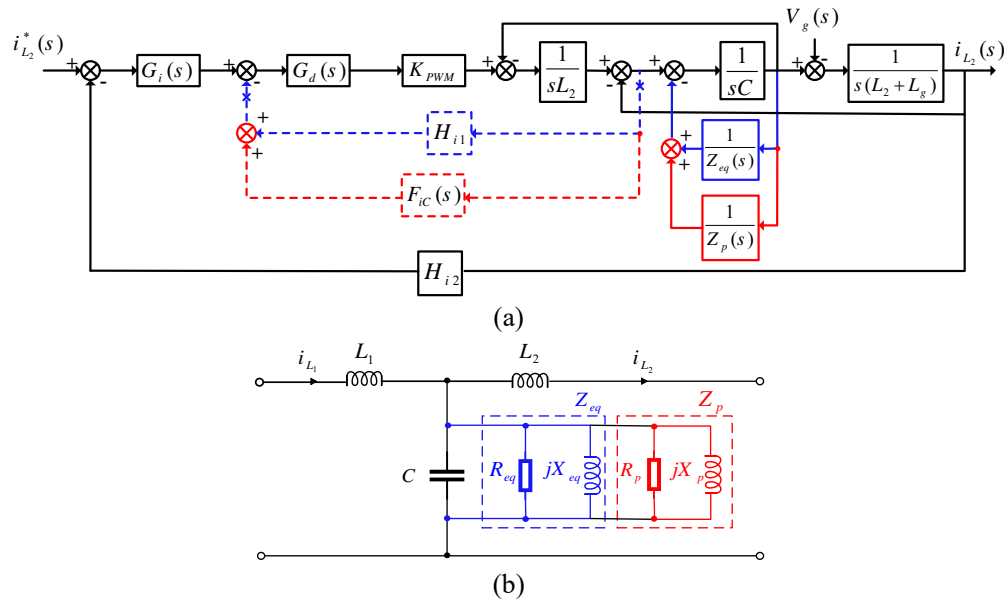
Fig. 7: Scheme of the grid-tied inverter with added parallel impedance, (a) diagram of the control system, (b) equivalent circuit

Z_p can be a parallel connection between the R_p resistor and the X_p reactance. Accordingly, the R'_{eq} and X'_{eq} are the equivalent resistance and the equivalent reactance, respectively, which are expressed in the following way:

$$R_{eq}'(\omega) = R_{eq}(\omega) \,||\, R_p(\omega) = \frac{R_{eq}(\omega)R_p(\omega)}{R_{eq}(\omega) + R_p(\omega)} \tag{10}$$

$$X_{eq}'(\omega) = X_{eq}(\omega) \,||\, X_p(\omega) = \frac{X_{eq}(\omega)X_p(\omega)}{X_{eq}(\omega) + X_p(\omega)} \tag{11}$$

R_p and X_p depend on frequency. Based on (10), a favorable R_p can help ensure a positive R'_{eq} over the entire range of controllable frequencies. To achieve this, an appropriate feedback function of the capacitor-current must be chosen.

3. 2. Proper performance of capacitor-current feedback

Based on Fig. 7(a), the CCF function consists of H_{i1} and F_{iC}. This means that a good F_{iC} is required to comply with H_{i1}. Basically, different types of FiC can be chosen. Nevertheless, the simple and common integral expression is $F_{iC}(s) = K/s$, K is the integral coefficient in this case. As a result, a proportional-integral controller (PI) is used to feed the capacitor current. Here, the H_{i1} and K symbols must be similar. Otherwise, the feedback function has a complex right half-plane zero (RHP), which results in a non-minimum phase characteristic. As a result, the examination of the two cases should be considered according to Table (1).

Fig 7(a) illustrates the equivalent block diagram that enables easy extraction of the R_P expressions associated with the integral term, presented in Table (1). Fig. 8 illustrates the R_{eq} and R_p frequency characteristics for the proportional-integral controller in two K> 0, $H_{i1}> 0$ and K<0, $H_{i1} <0$ modes. As shown in Fig. 8(a), in the [$f_{sam}/3$, $f_{sam}/6$] frequency range, resistors R_{eq} and R_p are both negative; therefore, R'_{eq} should be negative according to (10). This means that condition (a) does not create favorable conditions. As displayed in Fig. 8(b), in the [$f_{sam}/3$, $f_{sam}/6$] frequency range, the resistors R_p and R_{eq} are both positive, so R'_{eq} is positive definite. In Fig. 8(b), R_{eq} and R_p have opposite signs in other frequency ranges. Based on Equation (10), R'_{eq} is positive if $R_{eq}+R_p<0$. By replacing the R_p and R_{eq} specified in Table (1) in the $R_{eq}+R_p=0$, the positive boundary frequency for R'_{eq}, which is shown as f_{Rb}, can determine that $H_{i1}/K=1.5T_s$, f_{Rb} is approximately equal to $0.48f_{sam}$. This means that the upper limit of the frequency range for the positive R'_{eq} is increased to approximately $f_{sam}/2$. Consequently, the AD of the positive CCF exhibits good performance using the proportional-integral controller $H_{i1} + K/s$ (K <0, $H_{i1} <0$).
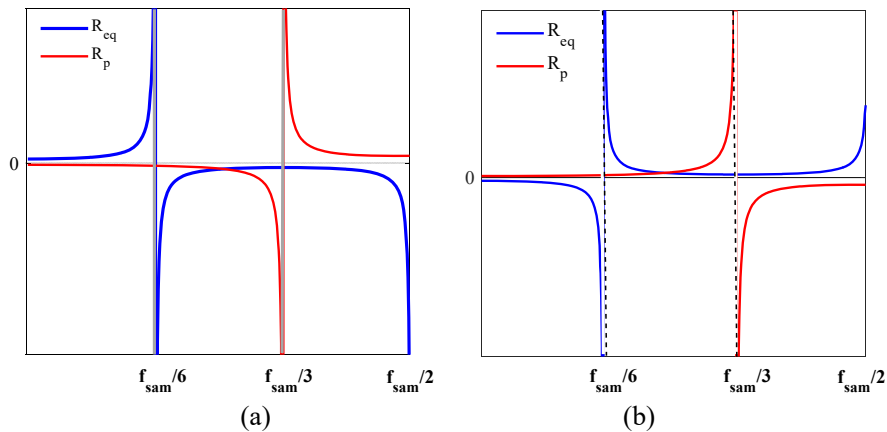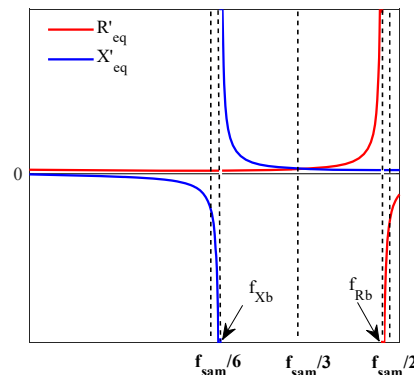

Fig. 8: Frequency response characteristic of R_{eq} and R_p in the presence of proportional-integral controller in the positive CCF path (a) $H_{i1}> 0$, K> 0, (b) $H_{i1} <0$, K <0

Table 1: The range of positive equivalent resistance at its highest frequency with PI feedback

Feedback condition	$H_{i1} + K/s$	
	$K>0$, $H_{i1}>0$	$K<0$, $H_{i1}<0$
R_{eq}	$\dfrac{L_1}{H_{i1} K_{pwm} C \cos(1.5\omega T_s)}$	
R_p	$-\dfrac{L_1 \omega}{K \cdot K_{pwm} C \sin(1.5\omega T_s)}$	
The maximum frequency range of positive R'_{eq}	$(0, f_{sam}/6)$ or $(f_{sam}/3, f_{sam}/2)$	$(0, f_{sam}/2)$

3. 3. Active damping based on positive proportional-integral capacitor-current feedback

R'_{eq} and X'_{eq} frequency characteristics for the AD of the positive proportional-integral CCF are plotted in Fig. 9. According to this figure, R'_{eq} has a positive value in the $[0, f_{Rb}]$ and a negative value in the $[f_{Rb}, f_{sam}/2]$ frequency range. X'_{eq} has capacitive properties in the $[0, f_{Xb}]$ and inductive properties in the $[f_{Xb}, f_{sam}/2]$ frequency range, in which f_{Xb} represents the boundary frequency of X'_{eq}. As mentioned, the maximum frequency of the positive equivalent resistance, f_{Rb}, has increased by nearly $f_{sam}/2$. Thus, a minimum phase response of the system is guaranteed, which leads to an increase in the stability of the grid-connected inverter against the network impedance changes.

Fig. 9: Frequency characteristic of R'_{eq} and X'_{eq} for the positive proportional-integral CCF AD

4. Design of control parameters

According to the topics discussed in Section 3, the controlling parameters of the CCF function and the current regulator must be adjusted correctly to ensure $R_{eq}(f_r')> 0$. This section presents the control parameters design.

4. 1. Decoupled two-loop model

The loop gain T(s) demonstrated in (3) is rewriteable as follows:

$$T(s) = \frac{H_{i2}G_i(s)}{s^2(L_2 + L_g)C} \cdot \frac{G_{iC}(s)}{1 + H_{i1}(s)G_{iC}(s)} \qquad (12)$$

In which:

$$G_{iC}(s) = \frac{K_{pwm}G_d(s)s}{L_1(s^2 + \omega_r^2)} \qquad (13)$$

Since the $G_i(s)$ current regulator does not have the imaginary axis right-half plane pole RHP, the number of RHP poles of loop gain is expressed by the following Equation:

$$\varphi_{iC}(s) = \frac{G_{iC}(s)}{1 + H_{i1}(s)G_{iC}(s)} \qquad (14)$$

As can be seen in (14), φ_{iC} is similar to a closed-loop system in that the feedforward and feedback transfer functions are $G_{iC}(s)$ and $H_{i1}(s)$, respectively. By considering equations (12) and (14), it is possible to construct an equivalent control diagram according to Fig. 10. If the internal loop is stably designed, the external loop will not include the open-loop right pole. Therefore, in the Nyquist stability discussion, the number of right half-plane poles of the open-loop conversion function will be zero (P = 0). Hence, the internal loop parameters or the CCF parameters can be designed independently to warranty P = 0. Afterward, the external loop parameters or the same parameters of the current regulator could be adjusted to guarantee system stability.

Fig. 10: Equivalent control block diagram of the grid-connected inverter with LCL filter with positive proportional-integral CCF AD

4. 2. Capacitor-current feedback parameters design

Based on Fig. 10, the $T_{iC}(s)$ internal loop gain is obtained as follows:

$$T_{iC}(s) = H_{i1}(s)G_{iC}(s) = \frac{K_{pwm}(H_{i1}s + K)}{L_1(s^2 + \omega_r^2)}e^{-1.5sT_s} \qquad (15)$$

Thus, the stability of the internal loop could be evaluated using Nyquist stability criteria, i.e., $P_i - 2(N_i(+) - N_i(-)) = 0$, where $N_i(+)$ and $N_i(-)$ present the number of positive and negative internal loop intersections, and P_i represents the number of right half-plane poles

(RHP) of the open-loop conversion function of the internal loop. As shown in (15), $T_{iC}(s)$ does not contain the RHP pole, and $P_i = 0$ is established. Therefore, $N_i(+) - N_i(-) = 0$ must be satisfied so that the internal loop is independently stable.

In Fig. 11, the Bode curves of the internal loop gain of (15) are shown. In the low-frequency range, the magnitude plot of $T_{iC}(s)$ has a zero slope, and the phase curve gradually decreases from 180° in the low-frequency range. In addition, when the filter resonant frequency (f_{res}) is reached, the magnitude curve shows an infinite resonance peak. The phase curve decreases in the corresponding frequency range and passes through the -180° at the f_{Rb} frequency. As a result, two gain margins, including GM_{i1} and GM_{i2}, must be observed to avoid negative zero-crossings at zero and f_{Rb} frequencies, respectively. Meanwhile, the PM_{i1} and PM_{i2} two-phase margins are defined at the crossover frequencies of phase f_{c_i1} and f_{c_i2}, respectively. In addition, with the realization of the PM_{i2} phase margin, the G_{Mi2} gain margin is automatically realized. Because the size of the open-loop conversion of the internal $T_{iC}(s)$ control loop decreases uniformly in the $[f_{c\_i2}, f_{sam}/2]$ frequency range.
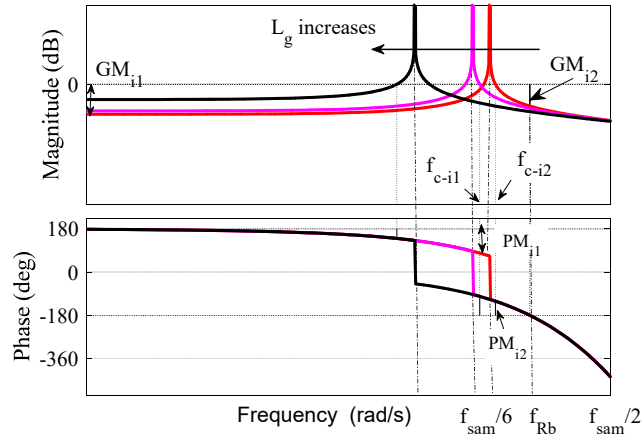

Fig. 11: Internal loop bode diagram of the positive proportional-integral CCF AD

Based on $GM_{i1} = -20lg \mid T_{iC}(j2\pi \cdot 0) \mid$, the boundary value of the coefficient K, which is limited by the gain margin of the internal loop, is obtained as follows:

$$K_{GM1} = 10^{\frac{GM1}{20}} \cdot \frac{L_1(2\pi f_{res})^2}{K_{pwm}} \tag{16}$$

Given that $PM_{i1} = \pi - \angle T_{iC}(j2\pi f_{c\_i1})$ and $PM_{i2} = \angle T_{iC}(j2\pi f_{c\_i2}) - (-\pi)$, the boundary value of the coefficient K in terms of H_{i1}, which is limited by the phase margins of the internal loop, is as follows:

$$K_{PMi1} = H_{i1} \cdot 2\pi f_{c\_i1} \cdot \tan(PM_{i1} - \frac{\pi}{2} - 3\pi f_{c\_i1} T_s) \tag{17}$$

$$K_{PMi2} = H_{i1} \cdot 2\pi f_{c\_i2} \cdot \tan(-PM_{i2} + \frac{\pi}{2} - 3\pi f_{c\_i2} T_s) \tag{18}$$

In which $f_{c\_i1,2}$ can be derived from $|T_{ic}(j2\pi f_{c\_i1,2})|=1$. Corresponding relationships with the $f_{c\_i1,2}$ phase intersection frequencies can be expressed using (19) and (20):

$$f_{c\_i1} = \frac{1}{2\pi}\sqrt{(2\pi f_{res})^2 + \frac{K_{pwm}^2 H_{i1}^2 - \sqrt{K_{pwm}^4 H_{i1}^4 + 4L_1^2 K_{pwm}^2 H_{i1}^2 (2\pi f_{res})^2 + 4L_1^2 K_{pwm}^2 K^2}}{2L_1^2}} \quad (19)$$

$$f_{c\_i2} = \frac{1}{2\pi}\sqrt{(2\pi f_{res})^2 + \frac{K_{pwm}^2 H_{i1}^2 + \sqrt{K_{pwm}^4 H_{i1}^4 + 4L_1^2 K_{pwm}^2 H_{i1}^2 (2\pi f_{res})^2 + 4L_1^2 K_{pwm}^2 K^2}}{2L_1^2}} \quad (20)$$

Considering that the approximation $\tan(3\pi f_{c\_i1,2}2T_s)\approx\tan(3\pi f_{res}T_s)$ is valid due to the proximity of the gain crossover frequencies $f_{c\_i1,2}$ to the filter resonant frequency f_r, by replacing (19) and (20) in (17) and (18), respectively, Equation (21) is obtained:

$$K_{PMi1,2} = -\sqrt{\left(4\pi^2 \lambda_{1,2}^2 f_{res}^2 H_{i1}^2 + \frac{(\lambda_{1,2}^4 + \lambda_{1,2}^2)K_{pwm}^2 H_{i1}^4}{2L_1^2}\right) + \sqrt{\left(4\pi^2 \lambda_{1,2}^2 f_{res}^2 H_{i1}^2 + \frac{(\lambda_{1,2}^4 + \lambda_{1,2}^2)K_{pwm}^2 H_{i1}^4}{2L_1^2}\right)^2 - (4\pi^2 f_{res}^2 L_1 H_{i1})^2}}$$

$$(21)$$

In which:

$$\lambda_1 = \tan(\frac{\pi}{2} + 3\pi f_{res}T_s - PM_{i1}) \qquad\qquad 21.\,a$$

$$\lambda_2 = \tan(-\frac{\pi}{2} + 3\pi f_{res}T_s + PM_{i2}) \qquad\qquad 21.\,b$$

If GM_{i1}, PM_{i1}, and PM_{i2} are specified, an acceptable range of K in terms of H_{i1} is determined from (16) and (21). In addition, the optimum phase and gain margin for the internal loop must be satisfied throughout the L_g network impedance range. As shown in Fig. 11, with increasing L_g, the values of GM_{i1} and PM_{i1} decrease, and PM_{i2} increase. This means that the satisfactory range boundaries for the K coefficient should be obtained respectively by GM_{i1} and PM_{i1} at the maximum value of L_g and by PM_{i2} at the minimum value of L_g. The gain and the phase margin should not be less than 3 dB and 30°, respectively [27].

4.3. Current regulator parameters design

Three parameters ω_i, K_p, and K_r, must be designed based on Equation (2). To deal with ±1% changes in the base frequency of the network [8], $\omega_i = \%1\times2\pi f_o = \pi$ rad/s is set. K_r and K_p are generally set assuming $L_g = 0$ [25]. By assuming $|T(j2\pi f_c)| = 1$, the value of K_p bounded by f_c is calculated [28], which can be expressed by Equation (22):

$$K_p \approx \frac{2\pi f_c(L_1 + L_2)}{H_{i2}K_{pwm}} \qquad\qquad\qquad (22)$$

To lessen the phase delay of the PR controller at the gain crossover frequency, the $G_i(s)$ corner frequency should be set to 10% of the gain crossover frequency f_c [29]. As a result, the optimal K_r is equal to the following relation:

$$K_r = \frac{2\pi f_c}{10} \cdot \frac{K_p}{2\omega_i} \tag{23}$$

Based on (22) and (23), the appropriate K_p and K_r are determined based on the value of f_c. The highest possible value of f_c is constrained by the desired PM so that, considering $f_c \approx 4f_{sam}$ with a phase limit (PM) of approximately 60 degrees, creates a favorable condition, and a small percentage of overshoot is expected under these conditions [30]. In the next step, it is essential to examine the external loop gain margin (GM). If the required conditions are not satisfied at the external loop gain margin, f_c must be readjusted, which will correct the K_p and K_r values.

5. Sample design and simulation results

5. 1. A sample system design

Table 2 presents the parameters of a 6 kW single-phase LCL grid-connected inverter. For the evaluation of the proposed damping method, a high resonant frequency LCL filter $f_{r0} = 6.27$ kHz was utilized. The robustness of the system has been investigated by changing the L_g to 10% per unit, which is equivalent to 2.6 mH. Given the above values for the internal loop gain and phase margin, the acceptable area for K and H_{i1} can be plotted as depicted in Fig. 12. It can be observed that the area enclosed by the blue, red, and purple lines offers an optimal range for selecting the H_{i1} and K parameters. Any point within this region can be considered as suitable values for the H_{i1} and K parameters. Suitable parameters $H_{i1} = 0.06$ and K = 1600 are selected, corresponding to point A. By replacing $f_c \approx \%4f_{sam} = 800$ Hz into (22) and (23), $K_p = 0.7158$ and $K_r = 57.2610$ are computed.

Table 2: The values of the under-consideration system parameters.

| Parameter	Symbol	Value
Grid voltage	V_g	220 V
Output power	P_o	5.8 KW
Base frequency	f_o	50 Hz
Switching frequency	f_{sw}	10 KHz
Resonance frequency	f_{res}	6.27 KHz
Sampling frequency	$f_s=f_{sam}$	20 KHz
Inverter side inductor	L_1	826 μH
Grid side inductor	L_2	200 μH
Filter capacitor	C	4 μf
DC link capacitor	C_{DC}	6000 μf
Triangular carrier signal amplitude	V_{tri}	4.58 V
Grid current sensor gain	H_{i2}	0.15
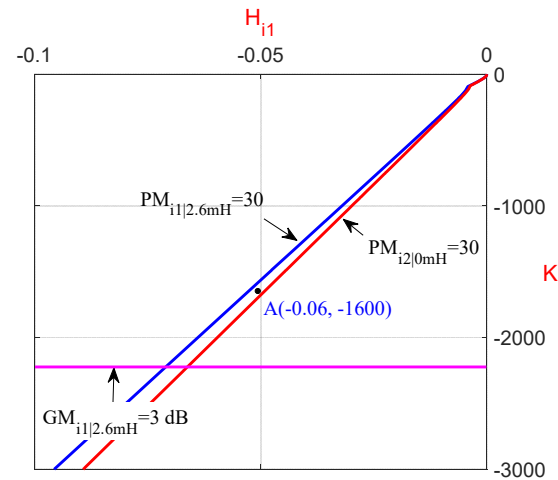
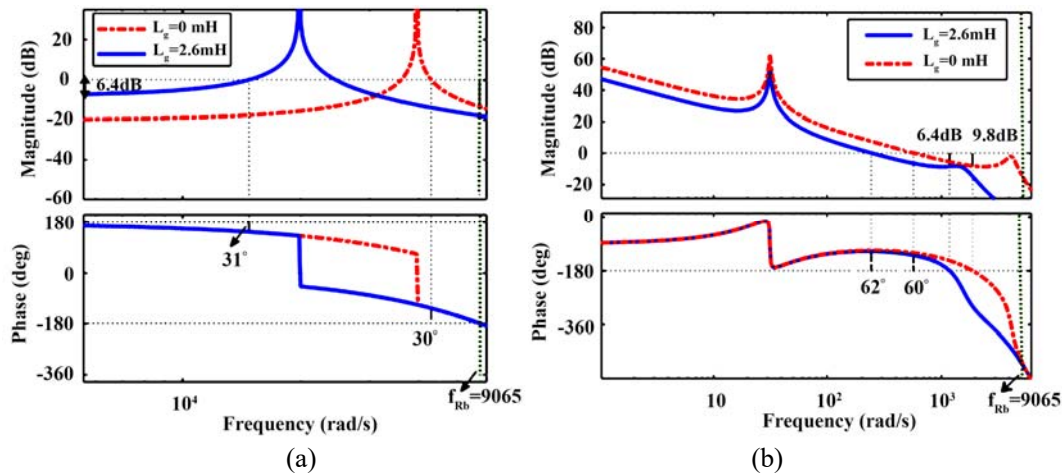Fig. 12: Satisfactory and stable region for H_{i1} in terms of K

(a)

(b)

Fig. 13: Bode diagram of a two-loop system, (a) internal loop gain, (b) external loop gain

Based on the defined parameters, the internal and external loop diagrams can be illustrated according to Fig. 13. Based on this figure, the minimum gain of the internal loop and the phase margin under the condition that the network impedance L_g=2.6 mH are 6.4 dB and 31°, respectively. In contrast, the minimum gain of the external loop of the gain margin and phase margin in the same condition are 6.4 dB and 62°, respectively. In addition, the minimum gain of the external loop of the phase and the gain margin, in the case of L_g=0 mH, are 60 degrees and 9.8 dB, respectively. Thus, both loops have good stability margins, and this confirms the effectiveness of the design method.

Fig. 14 demonstrates the distribution of open loop and closed loop poles based on the change in L_g grid impedance from 0mH to 2.6mH. In this analysis, the closed-loop pole pair

resulting from the PR regulator is not shown due to their small changes. As displayed in Fig. 14(a), both pairs of inverter's open loop poles with the proportional-integral CCPF damping method are always inside the unit circle and lead to P≡0. Fig. 14(b) shows that the closed-loop poles of the inverter with the proportional-integral CCPF damping are inside the unit circle, far from its boundaries. Based on this, a sufficient stability margin is obtained using this damping method even for f_{res} close to or equal to $f_{sam}/6$. Therefore, the proportional-integral CCPF damping method increases the inverter stability during the changes in network impedance and improves dynamic performance.
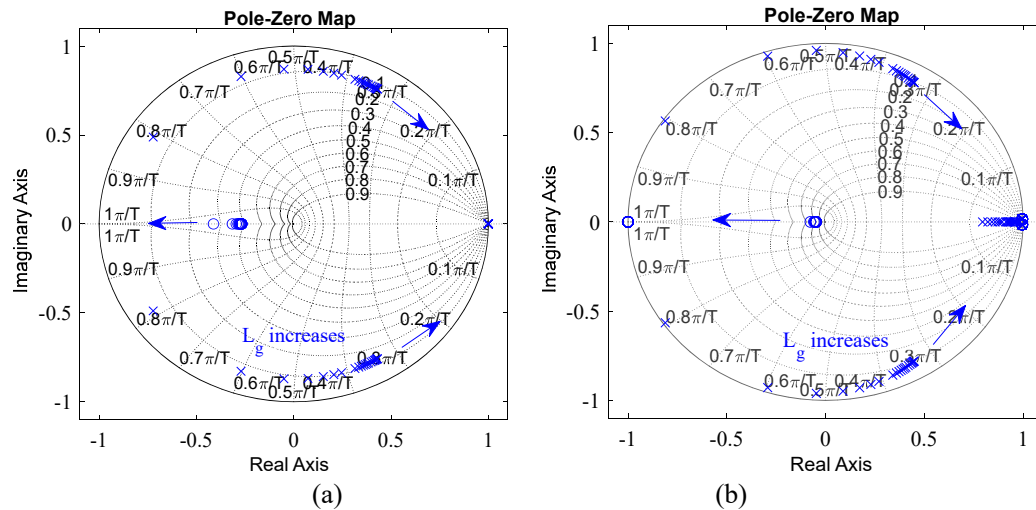
Fig. 14: Grid-connected pole-zero map with changes in network impedance, (a) open loop pole-zero map, (b) closed loop pole-zero map

5. 3. Simulation results

This section presents simulation results of PEMFC power injection into the weak grid using the proposed control system. Simulations are performed using a 6 kW-45 V PEMFC stack. To model the mentioned conditions and verify the reliability of the proposed control system, the network impedance is considered as 0 mH and 2.6 mH. The worst-case network impedance is pure inductance, which is modeled with a value of 2.6 mH. In Fig. 15-a and b, the P-I and V-I curves of the PEMFC stack can be seen. As shown in Fig. 15-a, with the increase in power produced by the PEMFC, the current also increases, but as the current increases, the voltage produced by the PEMFC decreases, as shown in Fig. 15-b.
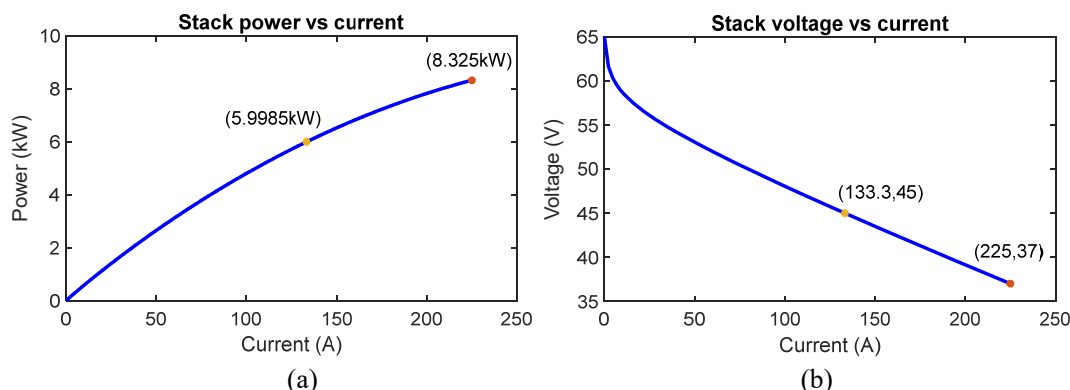
Fig. 15: PEMFC P-I and V-I curves (a) P-I curve, (b) V-I curve

Fig. 16 shows the fuel flow rate and the voltage produced by the PEMFC. As shown in Fig. 16-a, the fuel flow rate has decreased by 20% in the time interval [0.8s, 1.2s]. As a result, the voltage produced by the PEMFC has also decreased in the previous time interval, as shown in Fig. 16-b. Since the PEMFC produces a low voltage, a boost converter is used to increase it. Fig. 17 shows the DC link voltage of the inverter. It is evident from Fig. 17 that the DC link voltage changes are very small in the [0.8s, 1.2s] time interval. It is also clear that the voltage ripple of the inverter DC link is very low.
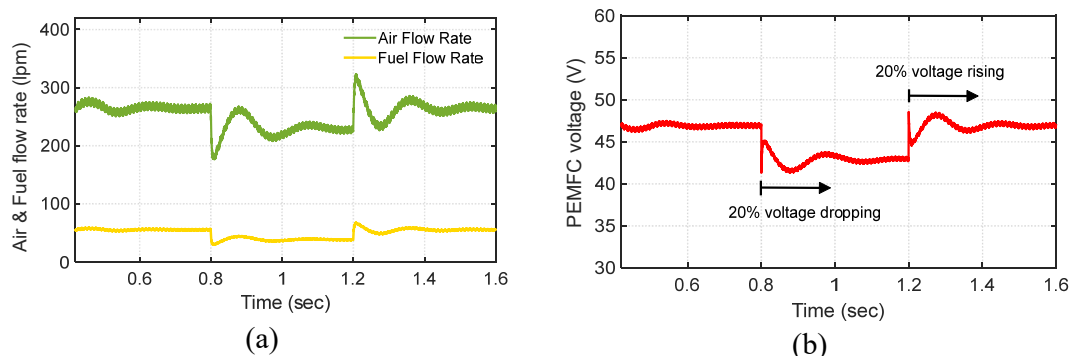

Fig. 16: (a) Fuel and air flow rate, (b) PEMFC output voltage
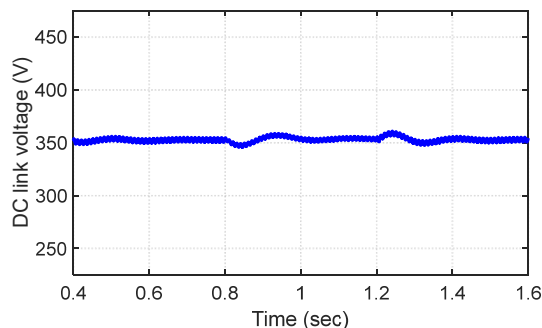

Fig. 17: Inverter DC link voltage

Grid-connected control systems aim to inject sinusoidal current into the network. Fig. 18 shows the injected current in the network at two impedance values, L_g=0 mH and L_g=2.6 mH. According to Fig. 18, the injected current into the network maintains its sinusoidal waveform at both values of the network impedance and when the injected power into the system changes.
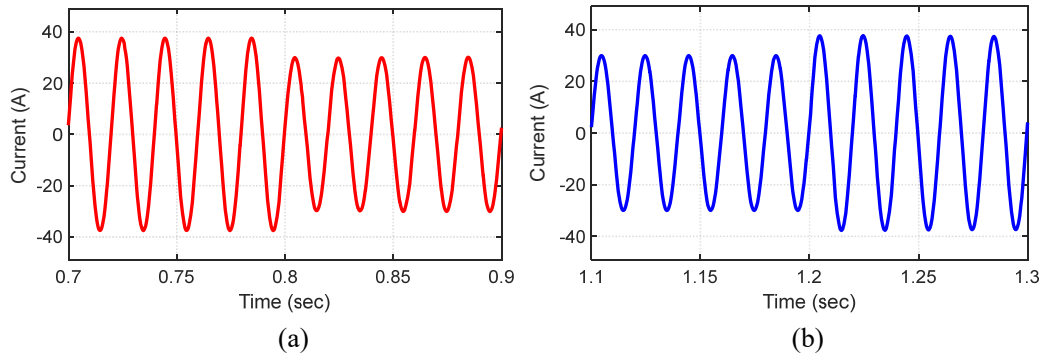

Fig. 18: The waveforms of the injected current into the network (a) L_g=0 mH, (b) L_g=2.6 mH

The network voltage and current waveforms for L_g=2.6mH are shown in Fig. 19-a. This figure shows that as the PEMFC fuel flow rate is reduced, the produced power will also be reduced within the [0.8s, 1.2s] time interval. During this condition, the network voltage and current maintain their sinusoidal waveform. Fig. 19-b shows the voltage and current waveforms in the [0.94s, 1.05s] time interval. It is clear that the voltage and current waveforms are sinusoidal, and there is no phase difference between them.
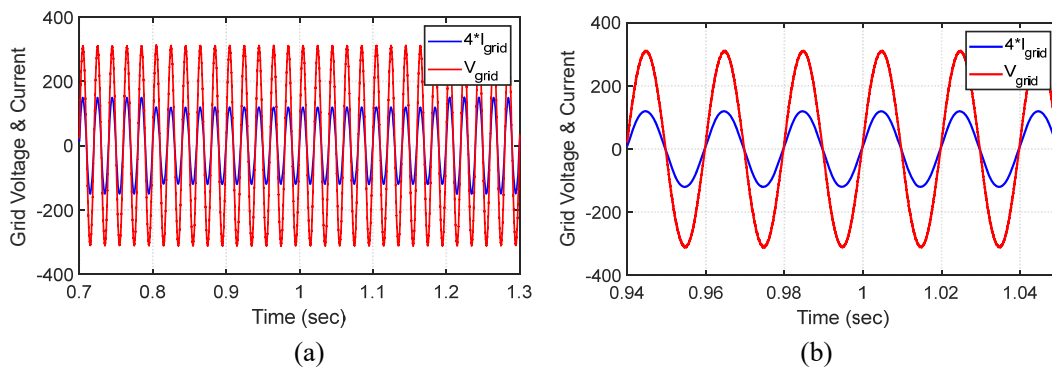

Fig. 19: Network voltage and current waveforms in the (a) [0.7s, 0.1.3s] time interval, (b) [0.94s, 1.05s] time interval

The THD of the network current is shown in Fig. 20, and its value is 0.96% for L_g=2.6mH and 1.56% for L_g=0mH. According to Fig. 20, it is clear that the proposed method for the worst condition of the network, i.e., L_g=2.6mH, maintains its stability and has a lower THD than the normal conditions of the network.
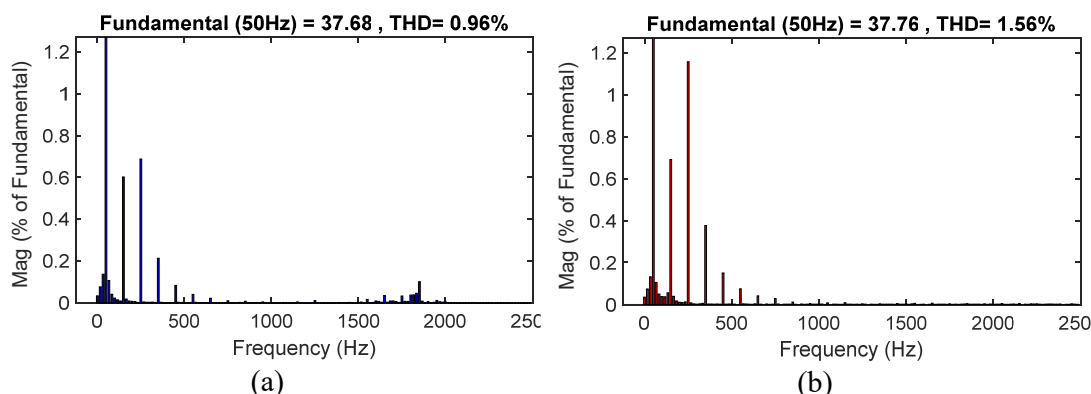
Fig. 20: Network current THD (a) L_g=2.6 mH, (b) L_g=0 mH.

Fig. 21 illustrates the injected power into the network. Due to the reduction of the power produced by the PEMFC in the [0.8s, 1.2s], the injected power into the network has also decreased from 5800 W to 4650 W in the same time interval.
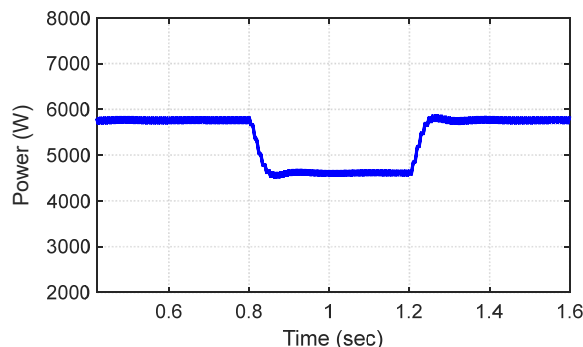

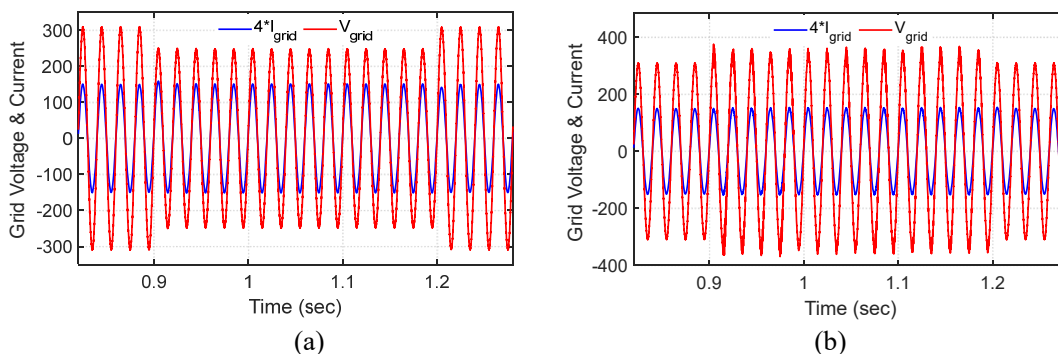Fig. 21: The waveform of the injected power into the network

Fig. 22: Grid voltage and current waveforms when (a) network voltage drops by 20%, (b) network voltage rises by 10%

Fig. 22 shows a fluctuation in the network voltage. In Fig. 22-a, the network voltage has dropped by 20% in the [0.9s, 1.2s] time interval. As the network voltage drops, the current waveform is sinusoidal and has no phase difference from the network voltage. In the case that the network experiences a voltage rise of up to 10% in the [0.9s, 1.2s] time interval, it

can be seen in Fig. 22-b that the system remains stable and that there is no phase difference between the system and the network voltage.

At the end, a comparison between the proposed method and the methods that have recently been proposed in the field of improving the performance of the grid-connected inverter control system is presented in Table 3 The references included in this table were evaluated based on their THD of the injected current into the grid, considering the assumed conditions of each reference. By using the proposed method, it is evident that the current injected into the grid has a higher quality and a lower THD than others.

Table 3. Comparison of the proposed control scheme with other methods

	[32]	[33]	[34]	[35]	[36]	Proposed control scheme
Control method	Capacitor voltage feedback	LMI-LQR current control	Jaya	Grid side current feedback	Quasi-Predictive current control	Positive virtual impedance shaping
Grid side current THD	3.47%	2.43%	2.8%	4.82%	2.15%	1.56%

6. Conclusion

To dampen the resonance caused by the LCL filter in a grid-connected PEMFC system, a capacitor-current proportional-integral positive active damping method is proposed. The proposed method extends the frequency range of positive equivalent resistance up to Nyquist frequency, i.e., the full controllable frequency range, and eliminates the non-minimum phase behavior caused by negative resistance, which leads to improved system stability. As a result, the stability of the grid-integrated inverter against network impedance variations increases significantly. The proposed damping method uses the concept of equivalent virtual impedance of the grid-connected inverter to increase the stability and robustness of the system. To validate the effectiveness of the proposed method, several scenarios have been examined and a comprehensive evaluation conducted. Simulation results indicate that the proposed method for LCL filter resonance dampening in PEMFC grid-connected systems increases the stability of the grid-tied inverter against grid impedance variations and also results in the injection of high quality and low THD current into the grid.

Acknowledgment

References

[1] Inci, Mustafa. "Interline fuel cell (I-FC) system with dual-functional control capability." *international journal of hydrogen energy,* 45, no. 1, 891-903, 2020.

[2] Bornapour, Mosayeb, Rahmat-Allah Hooshmand, Amin Khodabakhshian, and Moein Parastegari. "Optimal coordinated scheduling of combined heat and power fuel cell, wind, and photovoltaic units in micro grids considering uncertainties." *Energy,* 117, 176-189, 2016.

[3] Inci, Mustafa, and Ömer Türksoy. "Review of fuel cells to grid interface: Configurations, technical challenges and trends." *journal of cleaner Production,* 213, 1353-1370, 2019.

[4] Li Sun, Yuhui Jin, Lei Pan, Jiong Shen, Kwang Y. Lee, " Efficiency analysis and control of a grid-connected PEM fuel cell in distributed generation", *Energy Conversion and Management*, 195, 587–596, 2019.

[5] Mohiuddin, S. M., Md Apel Mahmud, A. M. O. Haruni, and H. R. Pota. "Design and implementation of partial feedback linearizing controller for grid-connected fuel cell systems." *International Journal of Electrical Power & Energy Systems,* 93, 414-425, 2017.

[6] Yang, Yong, Xiaoqiang Guo, Zhigang Lu, Changchun Hua, Miguel Castilla, and Frede Blaabjerg. "Advanced control of grid-connected inverters for proton exchange membrane fuel cell system." *International Journal of Hydrogen Energy,* 45, no. 58, 33198-33207, 2020.

[7] Rasekh, Navid, and Majid Hosseinpour. "LCL filter design and robust converter side current feedback control for grid-connected Proton Exchange Membrane Fuel Cell system." *International Journal of Hydrogen Energy,* 45, no. 23, 13055-13067, 2020.

[8] Blaabjerg, Frede, Remus Teodorescu, Marco Liserre, and Adrian V. Timbus. "Overview of control and grid synchronization for distributed power generation systems." *IEEE Transactions on industrial electronics,* 53, no. 5, 1398-1409, 2006.

[9] Hosseinpour, Majid, Amin Kholousi, and Alireza Poulad. "A robust controller design procedure for LCL-type grid-tied proton exchange membrane fuel cell system in harmonics-polluted network." *Energy Science & Engineering,* 10, no. 10, 3798-3818, 2022.

[10] Liserre, Marco, Frede Blaabjerg, and Steffan Hansen. "Design and control of an LCL-filter-based three-phase active rectifier." *IEEE Transactions on industry applications,* 41, no. 5, 1281-1291, 2005.

[11] Hosseinpour, Majid, and Abdolmajid Dejamkhooy. "Control and power sharing among parallel three-phase three-wire and three-phase four-wire inverters in the presence of unbalanced and harmonic loads." *IEEJ Transactions on Electrical and Electronic Engineering* 13, no. 7, 1027-1033, 2018.

[12] Rasekh, Navid, Mohammad Mohsen Rahimian, Majid Hosseinpour, Abdolmajid Dejamkhooy, and Adel Akbarimajd. "A step by step design procedure of PR controller and capacitor current feedback active damping for a LCL-type grid-tied T-type inverter." In *2019 10th International Power Electronics, Drive Systems and Technologies Conference (PEDSTC)*, pp. 612-617. IEEE, 2019.

[13] Liu, Huaiyuan, Lei Li, Yuchao Liu, Dianguo Xu, and Qiang Gao. "Passivity based damping design for grid-connected converter with improved stability." *IEEE Access* 7, 185168-185178, 2019.

[14] Zhao, Tieying, Junran Li, and Ning Gao. "Capacitor-Current-Feedback With Improved Delay Compensation for LCL-Type Grid-Connected Inverter to Achieve High Robustness in Weak Grid." *IEEE Access*, 10, 127956-127968, 2022.

[15] Geng, Yiwen, Xuanfeng Song, Xu Zhang, Ke Yang, and Haiwei Liu. "Stability analysis and key parameters design for grid-connected current-source inverter with capacitor-voltage feedback active damping." *IEEE Transactions on Power Electronics,* 36, no. 6, 7097-7111, 2020.

[16] Rasekh, Navid, and Majid Hosseinpour. "Adequate tuning of LCL filter for robust performance of converter side current feedback control of grid connected modified–Y-source inverter." *International Journal of Industrial Electronics Control and Optimization,* 3, no. 3, 365-378, 2020.

[17] Wang, Xiongfei, Frede Blaabjerg, and Poh Chiang Loh. "Grid-current-feedback active damping for LCL resonance in grid-connected voltage-source converters." *IEEE Transactions on Power Electronics,* 31, no. 1, 213-223, 2015.

[18] Li, Weiwei, Xinbo Ruan, Donghua Pan, and Xuehua Wang. "Full-feedforward schemes of grid voltages for a three-phase LCL-type grid-connected inverter." *IEEE Transactions on Industrial Electronics,* 60, no. 6, 2237-2250, 2012.

[19] Harnefors, Lennart, Xiongfei Wang, Alejandro G. Yepes, and Frede Blaabjerg. "Passivity-based stability assessment of grid-connected VSCs—An overview." *IEEE Journal of emerging and selected topics in Power Electronics,* 4, no. 1, 116-125, 2015.

[20] Wang, Xiongfei, Frede Blaabjerg, and Poh Chiang Loh. "Grid-current-feedback active damping for LCL resonance in grid-connected voltage-source converters." *IEEE Transactions on Power Electronics,* 31, no. 1, 213-223, 2015.

[21] Hosseinpour, Majid, Mahastan Asad, and Navid Rasekh. "A Step-by-Step Design Procedure of a Robust Control Design for Grid-Connected Inverter by LCL Filter in a Weak and Harmonically Distorted Grid." *Iranian Journal of Science and Technology, Transactions of Electrical Engineering,* 45, no. 3, 843-859, 2021.

[22] Li, Xiaoqiang, Jingyang Fang, Yi Tang, Xiaojie Wu, and Yiwen Geng. "Capacitor-voltage feedforward with full delay compensation to improve weak grids adaptability of LCL-filtered grid-connected converters for distributed generation systems." *IEEE Transactions on Power Electronics,* 33, no. 1, 749-764, 2017.

[23] Hosseinpour, Majid, and Navid Rasekh. "A single-phase grid-tied PV based trans-z-source inverter utilizing LCL filter and grid side current active damping." *Journal of Energy Management and Technology* 3, no. 3, 67-77, 2019.

[24] Yin, Jinjun, Shanxu Duan, and Bangyin Liu. "Stability analysis of grid-connected inverter with LCL filter adopting a digital single-loop controller with inherent damping characteristic." *IEEE Transactions on Industrial Informatics,* 9, no. 2, 1104-1112, 2012.

[25] Rasekh, Navid, Majid Hosseinpour, Abdolmajid Dejamkhooy, and Adel Akbarimajd. "Robust power conditioning system based on LCL-type quasi-Y-source inverter for grid connection of photovoltaic arrays." *International Journal of Automation and Control,* 15, no. 6, 692-709, 2021.

[26] Pan, Donghua, Xinbo Ruan, Chenlei Bao, Weiwei Li, and Xuehua Wang. "Optimized controller design for LCL-type grid-connected inverter to achieve high robustness against grid-impedance variation." *IEEE Transactions on Industrial Electronics,* 62, no. 3, 1537-1547, 2014.

[27] Bao, Chenlei, Xinbo Ruan, Xuehua Wang, Weiwei Li, Donghua Pan, and Kailei Weng. "Step-by-step controller design for LCL-type grid-connected inverter with capacitor–current-feedback active-damping." *IEEE Transactions on Power Electronics,* 29, no. 3, 1239-1253, 2013.

[28] Liserre, Marco, Remus Teodorescu, and Frede Blaabjerg. "Stability of photovoltaic and wind turbine grid-connected inverters for a large set of grid impedance values." *IEEE transactions on power electronics* 21, no. 1, 263-272, 2006.

[29] Holmes, Donald Grahame, Thomas Anthony Lipo, Brendan Peter Mcgrath, and Wang Yui Kong. "Optimized design of stationary frame three phase AC current regulators." *IEEE transactions on power electronics* 24, no. 11, 2417-2426, 2009.

[30] Pan, Donghua, Xinbo Ruan, Xuehua Wang, Hui Yu, and Zhongwei Xing. "Analysis and design of current control schemes for LCL-type grid-connected inverter based on a general mathematical model." *IEEE Transactions on Power Electronics* 32, no. 6, 4395-4410, 2016.

[31] Association IS. Ieee std 519-2014. Recommended practice and requirements for harmonic control in electric power systems. IEEE Power Energy Soc 2014;29.

[32] Faiz, M. T., Khan, M. M., Jianming, X., Ali, M., Habib, S., Hashmi, K., & Tang, H. (2019). Capacitor voltage damping based on parallel feedforward compensation method for lcl-filter grid-connected inverter. *IEEE Transactions on Industry Applications*, *56*(1), 837-849.

[33] Bimarta, R., & Kim, K. H. (2020). A robust frequency-adaptive current control of a grid-connected inverter based on LMI-LQR under polytopic uncertainties. *IEEE Access*, *8*, 28756-28773.

[34] Padmanaban, S., Priyadarshi, N., Bhaskar, M. S., Holm-Nielsen, J. B., Hossain, E., & Azam, F. (2019). A hybrid photovoltaic-fuel cell for grid integration with jaya-based maximum power point tracking: experimental performance evaluation. *IEEE Access*, *7*, 82978-82990.

[35] Kim, Y. J., & Kim, H. (2019). Optimal design of LCL filter in grid-connected inverters. *IET Power Electronics*, *12*(7), 1774-1782.

[36] Dragičević, T., Zheng, C., Rodriguez, J., & Blaabjerg, F. (2019). Robust quasi-predictive control of LCL-filtered grid converters. *IEEE Transactions on Power Electronics*, *35*(2), 1934-1946.